Future Batteries 6 (2025) 100053

Contents lists available at ScienceDirect

Future Batteries

journal homepage: www.sciencedirect.com/journal/future-batteries

Performance assessment of all-solid-state lithium-ion cells with a novel solid polymer electrolyte: A multiscale modeling approach

Matteo Alberghini [a,*], Giulia Blanco [a], Ashutosh Agrawal [b,c], Pasquale Romano [d], Mattia Giuliano [d], Franklin Seute [e], Daniele Di Lecce [c,f], Ishamol Shaji [c,f], Giovanna Nicol [d], Alix Ladam [g], Sebastien Fantini [g], Mohammadhosein Safari [b,c,h], Philippe M. Vereecken [c,f], Alessio Tommasi [a]

[a] Gemmate Technologies, via Reano 31, 10090, Buttigliera Alta, Italy
[b] Institute for Materials Research (IMO-imomec), UHasselt, Martelarenlaan 42, B-3500 Hasselt, Belgium
[c] Energyville, Thor Park 8320, B-3600 Genk, Belgium
[d] C.R.F. SCpA, Strada Torino 50, 10043 Orbassano, Italy
[e] VDL Groep, Hoevenweg 1, 5652 AW, Eindhoven, The Netherlands
[f] Imec, Kapeldreef 75, Leuven, 3001, Belgium
[g] SOLVIONIC Company, 11 Chemin des Silos, 31100, Toulouse, France
[h] Imec, division IMOMEC, Hasselt, 3590, Belgium

ARTICLE INFO

Keywords:
All-solid-state batteries
Solid polymer electrolyte
Microscale modeling
Equivalent electrical circuit

ABSTRACT

Solid electrolytes are critical components in all-solid-state batteries. However, achieving high transport properties, compatibility with electrode materials, low cost, sustainability, and manufacturing compatibility remains a challenge. This work investigates the performance of a novel solid polymer electrolyte through an integrated approach combining experiments and numerical modeling. The electrolyte was tested for mechanical, electrochemical, and transport properties at different pressures, demonstrating good elasticity, high ionic conductivity, and adequate lithium diffusivity. Coin cells containing NMC622 and metallic Li were also fabricated and tested to evaluate its potential use with standard materials. To further investigate the cell behavior, a 3D-resolved model of the composite cathode was developed using a stochastic approach. The modeled microstructures were characterized in terms of connectivity, electrical conductivity, ionic tortuosity, and Young's modulus. A coupled electrochemical–mechanical model was then used to predict the cell performance operating with currents from C/20 to 1C. Compared to experimental voltammetry tests, the model showed good alignment. Furthermore, the parameters for an equivalent circuit model were derived from the microscale model and validated against dedicated experimental results, confirming its accuracy. The proposed multiscale modeling framework proved to bridge the gap between detailed microscale simulations and practical cell design, providing valuable insights into the optimization of solid-state cell architectures.

Introduction

All-solid-state batteries (ASSBs) promise to overcome the limitations of state-of-the-art liquid electrolyte cells. Most importantly, ASSBs improve cell safety, mainly due to their high thermal stability and low flammability [1,2]. They also significantly increase cell energy density by allowing the use of lithium metal as negative electrode [3]. Solid electrolytes offer good electrochemical stability, hinder the formation of dendrites [4], and enable the creation of miniaturized cells due to improved flexibility. Solid electrolytes can be either inorganic (e.g., argyrodite-type) or organic (e.g., solid polymeric electrolytes, SPEs). Compared to inorganic solid electrolytes, SPEs have lower transport properties and a limited temperature range. However, their strong adhesion and elasticity ensure good compatibility with electrodes, limited detachment during operation, and no requirement for high pressure [2]. In addition, their manufacturing and impregnation processes are easily scalable and can be implemented in existing manufacturing lines, facilitating their adoption in the current manufacturing industry. The development of novel SPEs require a comprehensive consideration of the entire cell assembly and the material behavior in the composite electrode. Key challenges slowing their use in commercial

* Corresponding author.
E-mail address: matteo.alberghini@gemmate-technologies.com (M. Alberghini).

https://doi.org/10.1016/j.fub.2025.100053
Received 30 September 2024; Received in revised form 8 January 2025; Accepted 26 February 2025
Available online 21 March 2025

applications include low adhesion with functionalized surfaces, poor mechanical properties, partial electrode infiltration due to high viscosity, and lower transfer properties compared to liquid counterparts [5]. Although testing different compositions is the most effective approach to advance this class of electrolytes, many operational aspects remain uninvestigated due to the difficulty and high cost of performing accurate microstructural characterizations, in-operando measurements, and precise post-mortem analyses.

In this context, simulations have proven to be fundamental in providing insight into the impact of the complex coupled physical phenomena involved in cell operation, allowing optimization of cell architectures while avoiding the fabrication of multiple samples and expensive characterizations. In addition, simulations can also validate the prospective use of novel technologies by predicting their scaled-up performance, focusing on specific applications. Among the various simulation techniques, microscale-resolved electrochemical simulations provide an accurate representation of the interplay between the various components in the cell, from polarization losses to predictive aging. Overall these simulations can be leveraged to guide the cells design or manufacturing process by offering detailed insights into cell performance. The simulated microstructure can be obtained through experimental characterization, physics-based simulation techniques, or stochastic approaches. A significant number of research studies have employed high-fidelity geometries with different purposes [6–10]. For instance, microstructures obtained via X-ray tomography were employed in the seminal work of Danner et al. [10] to perform FEM simulation of a full cell resolving all the solid cell phases (NMC, binder, carbon additive and graphite), proving the impact of inhomogenous carbon distribution on the cell performance. Similarly, Hein and co-workers [9] reconstructed the active material (AM) distribution in a real electrode and tested the effect of different numerical distribution strategies of a homogenized conductive binder to assess which modeling strategy results in the highest accuracy with respect to experiments. Other works have represented the electrode as stochastic assemblies of simplified geometrical objects [11–15]. This strategy has proved effective for optimizing the cell architecture by simplifying the acquisition of representative microstructures [11,15] or to assess the impact of the particles size and arrangement in ASSBs [14]. In contrast, discrete element method simulations can be used to assess the impact of the manufacturing process, such as calendering, on the resulting electrode microstructure and, consequently, performance [16,17].

Following these examples, this work combines experimental characterization and multiple modeling frameworks to assess the performance of an ASSB cell, which employs a novel SPE directly introduced in the electrode as a liquid precursor. The transfer properties of the SPE are experimentally evaluated under a range of applied pressures, consistent with typical working conditions. The characterization results are used as input parameters for a 3D-resolved microscale model of the full cell. The microstructure of the composite cathode was obtained using a stochastic approach recently proposed by some of the authors [11] and imported into the FEM software COMSOL Multiphysics® to assess the cell performance as a function of the applied current and internal stress distribution. Moreover, a comprehensive evaluation of the cathode properties is presented to validate the modeling approach. The cell performance obtained is then compared with experimental voltammetry tests performed on specifically manufactured coin cells, showing good agreement and providing fundamental insights into the cell's operating conditions and potential sources of mechanical degradation. Although full cell 3D simulations are highly accurate and well-representative, they often require extensive computation time and are therefore not suitable where rapid predictions are required, such as battery management systems, or for simulating long operating cycles with complex current patterns, such as those encountered in powertrain applications. Accordingly, the microscale model was also used to evaluate the parameters of an equivalent electrical circuit model (EECM), integrating the high representativeness of a 3D-resolved microstructure with the readily manageable EECM framework. The calibrated model parameters were compared with those obtained from dedicated pulsed power discharge tests on coin cells, validating the approach.

In conclusion, this work presents a comprehensive case study that integrates established methodologies within a multiscale modeling framework. By combining experimental characterization, microscale-resolved simulations, and EECM integration, we demonstrate how these techniques can be effectively applied to assess the performance of a specific all-solid-state battery architecture. This approach, while not introducing fundamentally new methods, showcases the value of systematically applying existing tools to gain deeper insights into cell performance and microstructure optimization while improving the model scalability.

Methods

Preparation and characterization of the solid electrolyte

The solid-polymer electrolyte (SPE) used in this work had composition of [(xM LiFSI in EMI FSI):PolyDDA FSI] [60:40 wt%], with LiFSI being lithium bis(fluorosulfonyl)imide salt with concentrations x of 1M and 3M, used respectively as separator and as catholyte. First, polymer electrolyte solutions were prepared by dissolving LiFSI, EMIFSI, and polydiallyldimethylammonium (polyDDA) FSI in acetonitrile. Free-standing SPE sheets (see Fig. 1A) were produced by casting the as-prepared polymer electrolyte solutions using a blade coating (Doctor Blade) in ambient conditions. Solvent evaporation was achieved by leaving the film in ambient conditions for 30 min. Afterwards, the membrane was dried in vacuum at 80 °C. To investigate the combined effects of pressure and electrochemical cycling on the SPE, a custom electrochemical pressure-cell setup was designed and manufactured as shown in Fig. 1B. This setup enables the measurement of the SPE stress–strain behavior and perform different electrochemical tests on Li|SPE|Li cells while applying a controlled external pressure. The air-tight split coin cell design allows to assemble and disassemble the setup in a pressurized environment, avoiding leakages and contamination. Force transducers (HBM, 0.1 kPa of resolution, 20 kPa of accuracy) and displacement sensors (Keyence, 0.1 μm of resolution, 1 μm of accuracy) were used to perform the stress–strain measurements and calibrated before each test. Cell assembly was performed in an argon-filled glove box (Mbraun), with oxygen and water vapor concentrations below 1 ppm. All measurements were performed at 25 °C.

The ionic transport properties of the SPE were evaluated via electrochemical impedance spectroscopy (EIS) while applying pressures of 1 MPa, 2.5 MPa and 5 MPa. The frequency range of the applied voltages was varied between 1 MHz and 100 mHz with an excitation amplitude of 10 mV. The resulting Nyquist plot of the system electric resistance was used to evaluate the parameters of an equivalent single-branch RC circuit recovering the SPE behavior (see Fig. 1C).

The ionic conductivity of the SPE samples was determined from the high-frequency intercept of the real axis in the Nyquist plot (R_s in Fig. 1C). The SPE transference number was evaluated using the Bruce-Vincent method [18,19]. A small voltage bias $\Delta V = 8$ mV was applied to the symmetric cell and the current profile was recorded. In the absence of concentration gradients, the current flowing through the SPE can be evaluated as:

$$I_0 = \frac{\Delta V}{R_s + R_{p,0}}, \tag{1}$$

where R_s and $R_{p,0}$ are the SPE resistance prior to polarization (see Fig. 1C). Then, the measured current exponentially decreases from I_0 to the steady state value I_{ss}; at this stage, polarization also altered the interfacial SPE resistance, now evaluated as $R_{p,ss}$. Therefore, the transference number t_+ can be calculated as [18–20]:

$$t_+ = \frac{I_{ss}\left(\Delta V - I_0 R_{p,0}\right)}{I_0\left(\Delta V - I_{ss} R_{p,ss}\right)}, \tag{2}$$

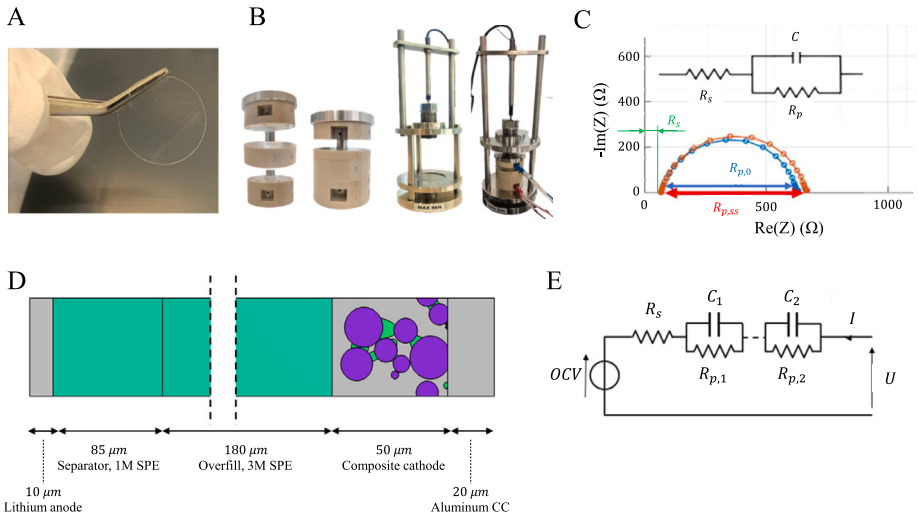

Fig. 1. Fabrication, characterization and modeling frameworks – adopted methodology: **(A)** Stand-alone solid-polymer electrolyte (SPE) sheets with composition of [(LiFSI in EMI FSI):PolyDDA FSI]. **(B)**) Pressure cell setup used to measure and control the stress and strain for the solid electrolytes and symmetric Li cells. **(C)** Schematics of the single-branch RC circuit representing the SPE electrical behavior. The Niquist plot, obtained via EIS measurements, can used to correct for the resistance of the passivation layers. **(D)** Schematics of a 50 μm × 50 μm 3D model resolved at the microscale representing the manufactured cell. The cathode geometry, comprising NMC622, carbon black, and CMC, was generated with a dedicated Octave script and imported in COMSOL Multiphysics® to perform electro-chemo-mechanical simulations. Dashed lines indicate the cut sections, allowing for an enlarged view of smaller components while maintaining the overall scale of the drawing. **(E)** Schematics of the 2-RC branches equivalent circuit model (ECM) used to represent the coin cell behavior. Note that the model parameters, fitted either on experimental or numerical data, are different with respect to those evaluated for the SPE and shown in panel C.

where Eq. (2) takes into account the correction due to the resistance of the passivation layers on the electrodes, evaluated by EIS directly before and after the Bruce-Vincent test. The electrolyte resistance R_s, in series with the electrode resistances $R_{p,o}$ or $R_{p,ss}$, was determined by fitting the EIS data to an equivalent circuit model (see Fig. 1C).

The Li diffusion coefficient in the SPE was evaluated by coupling the Newman method with the restricted diffusion technique [20]. The symmetric Li| SPE| Li cell was held under polarization for a couple of hours and then allowed to relax. Towards equilibrium, the logarithm of the cell open circuit voltage U during relaxation generally exhibits a linear behavior with respect to time. Therefore, the measured values of U can be related to the steady-state Li diffusion coefficient D by [20]:

$$-\frac{d\ln U}{dt} = \frac{\pi^2 D}{L^2}, \tag{3}$$

where L is the distance between the two electrodes.

Coin cell manufacturing and testing protocol

Three coin cells were manufactured using the novel SPE technology. The cell architecture comprised a nitrogen-treated, 20 μm thick Li film deposited by PVD on a 10 μm thick copper foil (Sidrabe). A self-standing SPE layer of (1M LiFSI in EMI FSI):PolyDDA FSI with nominal thickness of 85 μm was used as a separator. The cathode was composed by NMC622 (Umicore), carboxymethyl cellulose (CMC) as binder, and carbon black (Timcal-imerys c-nergy super C65). Doctor blade tape casting method was used to spread the cathodic slurry mixture on carbon-coated aluminium foil current collector (0.5 m/min, 270 μm of wet gap), which was then pre-dried at 110 °C. The resulting deposition presented a loading of 12.8 mg/cm^2, of which 92% was due to active material. Afterwards, the cathode was infiltrated by (3M LiFSI in EMIFSI):PDDAFSI in propylene carbonate via blade coating, including a layer of overfill above the electrode. The electrode was then dried in a vacuum oven (Buchi) at 55 °C for 5 days. The final SPE-infiltrated electrode presented a thickness of approximately 50 μm, plus an average SPE overfill of approximately 180 μm. The nominal resulting cell capacity was 3.54 mAh, with an equivalent nominal areal capacity of 2.00 mAh/cm^2.

The coin-cells were tested using two cyclometers (BasyTec XCTS); coin cell holders (Metrohm) were used to place the tested cells in a Falc climatic chamber (Falc) set at 25 °C to guarantee a constant temperature during the tests. The cells nominal capacity of 3.54 mAh was used as starting value for waking-up cycles: each cell underwent one cycle of charge/discharge at C/20 and then three cycles at C/10, where the C-rate was evaluated considering the nominal cell capacity, with 1C corresponding to 3.54 mA. The average discharge capacity measured during the three cycles at C/10 was considered as the effective cells capacity and used as reference for the subsequent tests. Constant-current voltammetry tests were performed considering C/20, C/10, C/5, C/2, 1C; three cycles were repeated for each current considered. Note that the C-rate considered in the voltammetry tests was evaluated for each cell based on the estimated cell capacity rather than on its nominal capacity.

3D-resolved microscale electrochemical–mechanical simulations

The cathodic cell microstructure was reconstructed using a dedicated numerical method based on the work by Alberghini et al. [11]. The active material (AM) was represented as an ensemble of spherical particles following a given particle size distribution, coherent with that provided by the NMC manufacturer (Umicore). The AM was distributed in a 50 μm thick cells, coherent with the experimental cathode thickness, with square cross section; the length of the square basis side was varied between 40 μm and 60 μm to assess the size independence of the resulting microstructure properties. Carbon black was represented by spherical particles with radius varying in the range 0.25 μm – 0.75 μm, randomly distributed on the NMC surface; AM particles were modeled as non-overlapping. Electrical conductivity was granted by the percolation provided by the carbon black aggregates. With respect to the original reference, the generation algorithm was improved to (i) include a polymeric binder, modeled as cylinders bridging neighboring particles [21], each with a radius randomly ranging from 20% to 60% of the minimum between the two particle radii it connects, and (ii) implement periodic boundary conditions for the active material. The volume fractions of materials considered within the cathode were evaluated from the experimental loading to maintain consistency with the manufacturing process, resulting in a 49.5% of NMC622, 4.7% of carbon black, 5.4% of CMC, and 40.4% of SPE; the latter was supposed to perfectly impregnate the cathode, filling all the

Table 1
Transfer properties of the 1M and 3M (LiFSI in EMI FSI):PolyDDA FSI solid polymer electrolyte (SPE) evaluated as a function of the applied pressure. For what concerns the compression tests, the SPE sample was initially 300 μm thick.

Pressure applied	1M SPE			3M SPE		
	1 MPa	2.5 MPa	5 MPa	1 MPa	2.5 MPa	5 MPa
SPE sheet thickness (μm)	284.17	209.61	171.01	290.05	219.96	183.73
Ionic conductivity (mS/cm)	0.2392	0.2741	0.3195	0.8077	0.8221	0.8745
Transference number (–)	0.1932	0.1951	0.1995	0.2092	0.2151	0.2274
Li diffusion coefficient (10^{-8} cm^2/s)	4.83	4.91	5.06	6.43	6.60	6.92

voids left by the other phases. The nominal cell capacity was set to 2 mAh/cm^2, consistent with the manufacturing targets. The geometries were generated by a dedicated Octave script and then imported into the finite elements software COMSOL Multiphysics® v6.2, which was used to perform the electrochemical–mechanical simulations: the simulation setup is outlined in Fig. 1D. In particular, the theoretical framework presented in Ref. [11] was extended to couple electrochemistry with solid mechanics [22–24], which allows to evaluate the internal cell stresses and consider the stress-induced Li transport within the AM. To this end, periodic boundary conditions were fundamental to correctly represent the internal stresses in the bordering NMC particles, which otherwise would lead to numerical instabilities. The mechanical model was solved supposing adhesion between all the phases included in the model. Cyclic voltammetry simulations were performed applying constant currents ranging from C/20 to 1C, considering upper and lower cutoff potentials of 4.3 V and 3.0 V, respectively. The AM was considered to be initially fully lithiated: the cell performance was evaluated after a few (dis)charge cycles, once steady state was reached. Note that the C-rate was evaluated considering the nominal cell capacity.

Equivalent electrical circuit model

The electrical behavior of the cell was modeled as a 2-branch RC model, which required the calibration of three resistance values and two capacitance values (see Fig. 1E). The model parameters were retrieved by numerical fitting either on dedicated experimental or simulated data: the two sets of parameters obtained would reproduce accurately the behavior of the experimental or the modeled cells.

On the experimental side, a dedicated discharge hybrid pulse power characterization (HPPC) test was performed: at constant intervals, the applied current, fixed at 1.326 A/m^2, was switched off and the system allowed to relax. The resulting time-depended cell voltage was used to fit the model parameters as a function of the average NMC relative lithium concentration θ, defined as the ratio between the average Li concentration in the active material and the maximum admissible concentration for NMC622 of 47,664 mol/m^3. Similarly, electrochemical FEM simulations of pulsed discharges at C/10 were performed on the 3D microstructure model, obtaining voltage relaxation curves for six different values of θ. The cell voltage U during relaxation in discharge tests can be analytically modeled as [25]:

$$U = I\,R_s + I\,R_{p,1}\left(1-\exp\left(\frac{-t}{C_1\,R_{p,1}}\right)\right) + I\,R_{p,2}\left(1-\exp\left(\frac{-t}{C_2\,R_{p,2}}\right)\right), \tag{4}$$

where $I = C/10$ is the applied current, R and C denotes the resistance and capacitance values as defined in Fig. 1E, and t is the elapsed test time. The fitting of the model parameters on the simulated cell performance was performed by minimizing the least squares error between Eq. (4) and the simulated relaxation curve as a function of the five model parameters. This procedure was repeated for the six θ-dependent curves evaluated.

Electrolyte characterization and cell performance

The results of the pressure-dependent SPE characterizations are summarized in Table 1.

The compression data of the SPEs can be used to assess the compression behavior of the SPE sheets in terms of their true strain. Analyzing the applied pressure as a function of the resulting true strain, an approximately linear relationship can be observed, suggesting that the SPE behaves as a linear elastic material in the pressure range considered. This allows to evaluate the Young modulus E of the SPE sheets as:

$$P = -E\ln\frac{L}{L_0}, \tag{5}$$

where P is the applied pressure, $-\ln L/L_0$ is the true strain and $L_0 =$ 300 μm is the initial SPE thicknesses. Eq. (5) was fitted by the least squares method on the experimental data considering a first-order polynomial imposing zero as y-intercept, which leads to $E = (8.4 \pm 0.8)$ MPa and $E = (9.7 \pm 1.1)$ MPa respectively for the 1M and 3M SPE. The Young's modulus values obtained were essential for evaluating the cell stress distribution in electrochemical–mechanical simulations and for estimating the SPE thickness when operating in a cell under compression.

The measured ionic conductivity varied with both pressure and concentration, with a more pronounced increase for lower LiFSI concentrations, within a range of 6% – 9.5% per MPa at 1M and in the range 1% – 2.5% per MPa at 3M SPE; as expected, the 3M SPE presented a conductivity +170% – +240% higher than the 1M. Importantly, the highest value of conductivity measured is in line with the best references reported in the literature [3,26,27]. Differently, the transference number t_+~0.2 presented minimal variations with pressure at 1M, and approximately +8% at 3M. The measured values of t_+ are in the lower range with respect to other polymer electrolytes reported in previous studies [26,27].

Finally, the Li diffusion coefficient presented minor variations with respect to pressure, with a maximum increase of +5% and +8% applying pressures of 5 MPa for the 1M and 3M SPEs, respectively. Higher concentrations of LiFSI increased the mobility of lithium ions, with an approximately 35% higher diffusivity for the 3M SPE. The peak measured value of D was $6.92\cdot10^{-8}$ cm^2/s on the 3M sample.

These findings are in line with previous references: the transport properties of a SPE under compression [28] or stretched [29] can be improved as a result of pore volume or defect reduction, alignment of polymer chains, and improved interaction between the polymer and Li ions. Furthermore, previous theoretical and experimental studies demonstrated that compression is able to improve the SPE transfer properties and, more generally, the cell performance and durability [30,31].

Fig. 2A shows an SEM image of the composite cathode in its uncompressed state, where the Al current collector, the composite cathode, the SPE overfill and their respective dimensions can be observed. As can be seen in the inset of the figure, the catholyte impregnation was not optimal, although it was difficult to estimate the amount of non-impregnated zones and their average size; even though only the cathode boundary is highlighted. This problem can be attributed to the suboptimal SPE impregnation procedure, which is expected to result in inhomogeneous performance among the different coin cells produced.

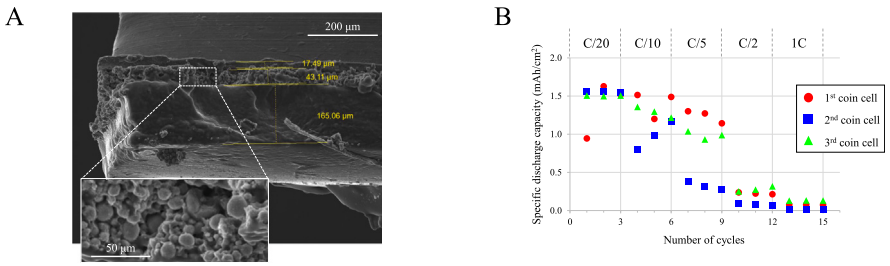

Fig. 2. Experimental investigation of the composite cathode and coin cells performance: **(A)** SEM image of the manufactured cathode **(B)** Specific discharge capacity measured on three manufactured coin cells operating at different C-rates. Three cycles are repeated for each C-rate considered.

In addition, the reduced NMC-SPE contact area is likely to limit the cell discharge capacity. The performance of the three coin cells was evaluated by galvanostatic voltammetry tests at different effecitve C-rates, with three discharge cycles per C-rate to assess performance stability. The main results are shown in Fig. 2B. As it can be observed, the specific discharge capacity of the 1st and 3rd cells is similar and fairly constant throughout the different runs, while that of the 2nd cell drops for C/10 or higher currents. The performance of all cells decreased when C/2 or higher currents were applied. Notably, the maximum capacity measured was about 1.6 mAh/cm^2, approximately 20% lower than the nominal cell capacity, which can be used as an estimate of the impact of manufacturing defects such as the non-ideal SPE impregnation (see Fig. 2A). Further tests showed that the best performing coin cells are able to maintain 95% of their capacity after 7 cycles at C/20. Besides discharge capacity, cyclic voltammetry tests alone offer limited insight into the cell internal operating conditions. Numerical simulations, on the other hand, can provide additional information about lithium transfer, possible degradation mechanisms, and optimization strategies. To this end, the following Sections analyze the performance of a composite cathode microstructure obtained through a numerical generation algorithm, assuming perfect SPE impregnation. The obtained microstructure was then used to evaluate the cell capacity through electrochemical simulations and compared with the experimental results.

Simulated cathode microstructures: analysis and key properties

Accurate cathode representation at the microstructure level is crucial for reliable cell performance prediction: the properties of the generated microstructure were first analyzed using dedicated Octave scripts, including a size-independence study to balance accuracy and computational cost. For this purpose, 10 configurations are generated for each box size considered, aiming at statistical representativeness.

Overall, the results obtained show no significant dependence of the cathodic properties on the size of the simulation box in the considered range; as expected, the variance of the data decreases with increasing box size. All the configurations generated recovered the manufacturer particle size distribution with a maximum root mean squared error of 5% (see Fig. 3A). The hypothesis of non-overlapping particles implies that the electrical conductivity is granted by the percolation provided by the carbon black aggregates: particles not connected to the networks are isolated and cannot participate to Li de/intercalation (see the schematics in Fig. 3B). The percentage of NMC particles not connected to the positive collector via carbon black (CB) remains stable at about (2 ± 2)%, suggesting an operating cell capacity close to the nominal value (see Fig. 3C). However, approximately (93 ± 1)% of the CB particles are located in areas that do not contribute to percolation: an interconnection of the AM well below the percolation threshold is likely to result in low electrical conductivity and therefore high ohmic losses during operation (see Fig. 3D). The presence of CB and CMC reduces the NMC/catholyte interface and increases the ionic tortuosity of the catholyte, resulting in lower efficiency (see the schematics in Fig. 3B). In the current cell model, the average NMC surface available for Li intercalation is approximately 50% (see Fig. 3E), with contributions from CMC and carbon black of (33 ± 3)% and (16 ± 1)%, respectively. This suggests that a higher concentration of CB should result in higher connectivity, thus increasing the cathodic electrical conductivity, while having little effect on Li intercalation. Instead, in the current configurations, CMC acts as a major intercalation inhibitor: cell performance could be improved by reducing its volume fraction, considering that the percentage of NMC connected to the positive current collector via CMC, and thus contributing to cathodic stiffness, is already stable at 98%–100% (see Fig. 3F).

Since the results presented confirm the box independence, a box size of 40 µm is considered; electrochemical simulations were performed on a single configuration reporting microstructural properties as close to the median as possible to ensure representativeness with the population analyzed.

Key performance indicators of the simulated cathodic microstructure were evaluated using dedicated FEM simulations. Effective cathodic conductivity is crucial to minimize ohmic losses during cell operation: to contrast the poor electrical conductivity of NMC of about 10^{-1} S/m, carbon conductive additive with conductivities in the order of 10^2 S/m are mixed. Generally, the CB network is modeled as homogeneously distributed within the catholyte domain: the common theoretical framework to evaluate the effective transport properties is the Bruggermann theory, which assumes a homogeneous distribution of spherical CB particles and estimated as $\sigma_{CB}(\phi_{CB}/(\phi_{CB} + \phi_{SPE} + \phi_{CMC}))^{1.5}$ [32–34], where ϕ denotes the volume fraction. Note that the SPE and CMC were assumed to be ideal electric insulators. This results in a percolation conductivity of ~2.8 S/m connecting all the AM particles directly to the positive current collector, leading to an overestimation of the cell performance [11]. In contrast, the proposed modeling framework provides an effective cathodic electrical conductivity of $3.8 \cdot 10^{-2}$ S/m, in line with other simulation studies of calendered electrodes [35]. The main difference between the estimates is due to the absence of conductive percolations, resulting in a longer average path for electron flow and the dominance of the AM conductivity over that of the CB. Furthermore, the results presented in Ref. [11] show a higher conductivity at almost the same volume fraction of AM and CB. This result captures the well-known role of AM size: particles in the range of 2 µm – 6 µm provide better connectivity than larger ones (here in the range of 5 µm – 25 µm). Since the effective electrical conductivity is crucial for estimating cell performance at higher currents, where ohmic losses play a critical role in cell failure and heat generation, building a model able to recover this parameter is fundamental for perspective technology upscaling.

The ionic tortuosity of the catholyte was estimated to be 1.7, which is in the lower-limit with respect to previous numerical results [35,36]. Note that the simulated tortuosity may be lower than its experimental counterpart due to the assumption of perfect electrolyte impregnation. The cathode Young's modulus was evaluated by applying it to the cell pressures ranging from −5 MPa to 5 MPa, with positive pressures being considered in traction. The assembly was also simulated under tensile stress to determine whether the elastic response was due to contact between adjacent AM particles (E ~140 GPa) or to the cohesive effect of

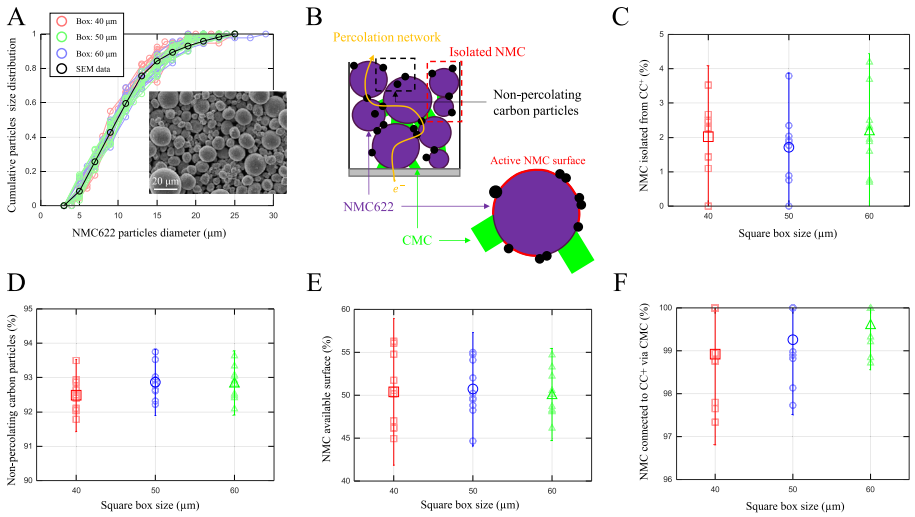

Fig. 3. Microstructural properties evaluated via open-source scripting and box size independence: **(A)** Comparison between the experimental (black data) and simulated (red, blue and green data) particle size distributions for the three different box sizes considered. **(B)** Schematics highlighting the relevant microstructure properties, impacting the cell performance, resulting from the microstructure generation algorithm and analyzed in the following panels. **(C)** Percentage of AM particles isolated from the positive current collector, therefore not able to participate to intercalation. **(D)** Percentage of carbon black particles included in the simulation box but not contributing to the percolation network. **(E)** Percentage of the AM surface interfacing with the solid polymer electrolyte. **(F)** Percentage of AM particles belonging to a cluster connected to the current collector via the polymeric binder. An AM cluster is defined by two or more particles connected via CMC. The results shown are obtained by generating 10 microstructures for each box size considered. The averaged values in panels C-F (larger markers, thick lines with error bars) are obtained by averaging the results for each individual configuration (smaller markers, thin lines without error bars).

the polymeric binder (E ~500 MPa), assuming that the NMC particles do not tend to overlap under tensile stress. The resulting data show symmetric linear behavior in compression and tension; interpreting the true strain-pressure curves with Eq. (5), the cathodic equivalent Young's modulus is 89.4 MPa. This suggests that the simulated mechanical response is due to the CMC network, which maintains cohesion and avoids pressure peaks due to AM-AM contact that could degrade NMC or SPE-AM cohesion.

The evaluated cathodic properties are critical for assessing the impact of modeling assumptions and provide a benchmark for future studies, while providing an opportunity to validate the proposed methodology.

3D-resolved full-cell simulations

Electrochemical–mechanical simulations were used to evaluate the simulated cell performance and to gain further insight into the effect of microstructure on several critical cell parameters. The results are then compared with the experimental voltammetry tests, providing a comparison between the model assumptions and the real cell architecture.

First, the nominal cell layout was modified to match the considered testing conditions. Coin cells were assembled using a manual hydraulic crimping machine, which applied a pressure during sealing slightly above 5 MPa: a compression of $P = -5$ MPa was also considered in the simulations. Accordingly, the thickness of the SPE separators and overfill was reduced following $L = L_0 \exp(P/E)$, which, considering the values of Young modulus evaluated in Section "Electrolyte characterization and cell performance", results in a thickness of 46.9 μm for the 1M separator, and 110.2 μm for the 3M overfill layer. The compression of the composite cathode was estimated to be less than 3 μm.

Electrochemical performance

Figs. 4A-B show the cell potential as a function of cell capacity and average relative Li concentration in the NMC (θ) for different applied current densities. Low C-rates allow deep discharges and high efficiencies: at C/20 the cell stores 1.94 mAh/cm^2 (see black curve, panel A), close to the nominal cell capacity, with a faradaic efficiency of 97.1%. The low applied current promotes lithium migration, allowing a wide θ window of 34%–97% (see black curve, panel B). As the current density was increased to C/10 and C/5 (red and blue curves, respectively), polarization losses slightly reduce the stored energy to 1.82 mAh/cm^2 and 1.65 mAh/cm^2, respectively. Further current increase leads to a significant decrease in cell performance, up to −62% at 1C (yellow data); simulating the setup with 2C or higher currents leads to cell failure with no stored or released energy. On the other hand, the faradaic efficiency of the cell remained higher than 95% for all tested conditions. Similarly, the available range of θ decreased progressively and was limited to 76%–90% at 1C (see Fig. 4B, yellow curve). Note that the operating θ ranges shown in Fig. 4B were obtained considering the cell as initially fully lithiated, in line with the experimental procedure. However, a different initial condition would have resulted in shifted operating ranges of θ and slightly different cell performance.

Different current densities also affect the homogeneity of the Li distribution across the cell. Fig. 4C shows the 3D relative Li concentration in the active material; instead, Fig. 4D shows the cross-sectional averaged Li concentration over the cathode length, starting from the positive current collector and moving toward the separator. Analysis of the 3D distribution shows that at C/20 Li is homogeneous within the solid and no variations are observed across the cathode thickness (Fig. 4D, black curves). Instead, cycling at 1C leads to pronounced inhomogeneity: smaller particles are quickly depleted of Li, increasing the cell potential closer to the cutoff, while larger particles still retain most of the lithium. However, the wide particle size distribution of AM results in the average lithium concentration being predominantly determined by the larger particles, without any particular variation across the cathode thickness (Fig. 4D, yellow curves). This result also highlights the importance of working with a narrow particle size distribution to achieve a uniform electrode behavior. Note that, despite the nominal cathode thickness of 50 μm the AM extends only up to 44 μm away from the current collector: this is due to the dense sphere packing obtained from the microstructure generation algorithm, which mimics the real cathode microstructure shown in Fig. 2A.

Analysis of internal stresses

The difference in lithium concentration also affects the mechanical behavior of the composite cathode during intercalation: lower currents

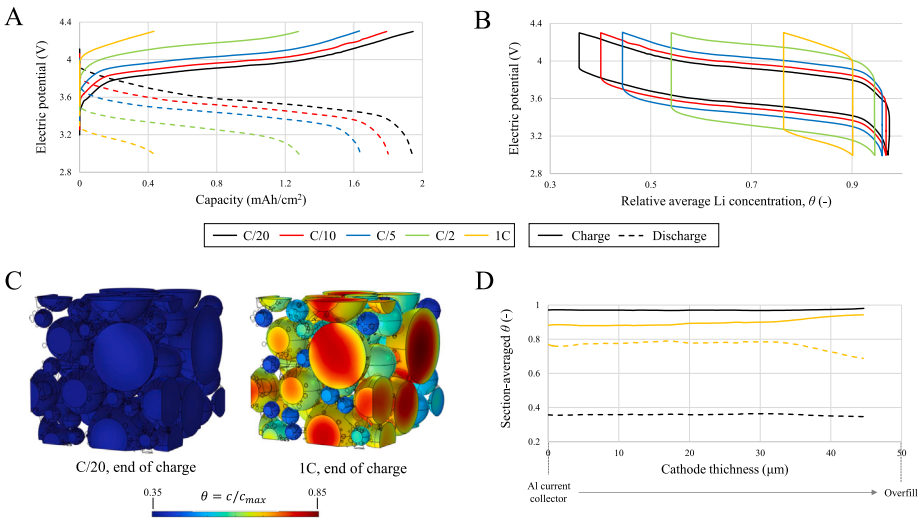

Fig. 4. Electrochemical performance – 3D simulations: **(A-B)** Cell voltage as a function of the cell capacity (panel A) or average relative Li concentration in the NMC (θ, panel B) when operating with different applied current densities. **(C)** 3D maps of the relative lithium concentration in the configuration investigated at the end of charging transient when operating with C/20 (left image) and 1C (right image). **(D)** Relative lithium concentration as a function of distance from the positive current collector. The results show the concentration profiles at the end of the charge (solid lines) and discharge (dashed lines) transients for C/20 (black data) and 1C (yellow data). The data were obtained by averaging the relative Li concentration in the NMC622 particles over the cross section.

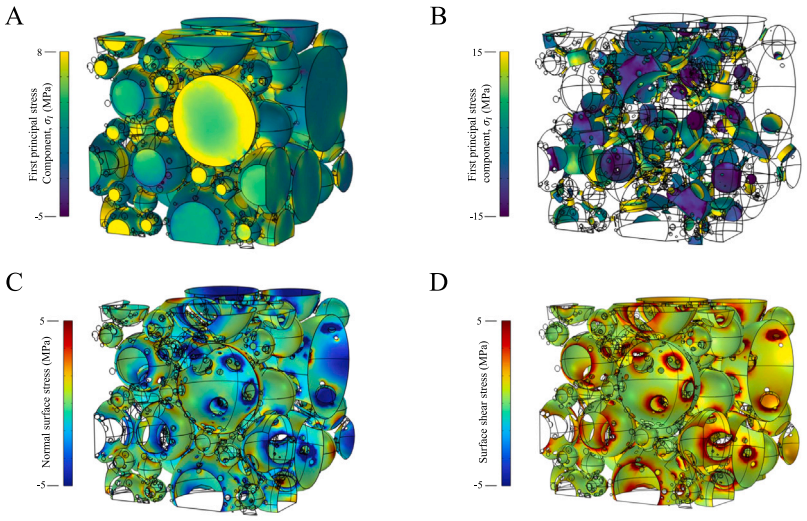

Fig. 5. Mechanical stress distribution – 3D simulations: **(A-B)** Maps of the first component of principal stress σ_I in the active material (panel A) and polymeric binder (panel B). σ_I is commonly related to mechanical failure of brittle materials. **(C-D)** Normal (panel C) and shear (panel D) surface stresses at the AM-SPE interface. Their combination is commonly related to detachment between cohesive surface. All the results presented are obtained at the end of the charging transient at C/20, namely at maximum AM contraction due to lithiun deintercalation.

result in deeper discharge rates and thus material contraction. This increases the first component of the principal stress σ_I in the AM, which is generally associated with crack propagation in brittle materials such as the NMC secondary particles. For this reason, the stress analysis was limited to the end of charging at C/20, which corresponds to maximum delithiation (see also Fig. 4B, black curve). As shown in Fig. 5A, complete cell delithiation results in an average σ_I of about +2 MPa, with regions up to +8 MPa at the current collector interface and around the NMC-binder interfaces, which resist NMC contraction. Note that in order to mimic the sealing of a button cell, the assembly was also under a compression of 5 MPa, thus providing a negative contribution to the principal stresses. These results show that pre-compressing the cell can mitigate the effects of de-lithiation and ultimately reduce material damage. They also suggest that the AM is unlikely to develop cracks, which are generally considered to propagate at σ_I ~100 MPa.

Instead, the binder is in a more mixed stress state with higher values of σ_I (see Fig. 5B), exhibiting regions in both tension and compression with peak values up to ±15 MPa. Two cases can be distinguished when analyzing the normal stress in Fig. 5B. Binder cylinders with axis (or longest dimension) approximately perpendicular to the current collector resist the external 5 MPa compression and are mostly under compression; instead, cylinders with axis (or longest dimension) mostly parallel to the current collector prevent material displacement during AM shrinkage and are mostly under tensile stress. However, these stresses are generally not considered sufficient to lead to failure, which in this framework is considered to occur at σ_I ~30 MPa [21,37]. Overall, therefore, the binder can be considered to be successfully contributing to the cohesion of the cathode without the risk of failure, even in the most severe working conditions considered.

The highly mixed stress condition in the binder network is crucial in determining the stresses at the NMC-SPE interface, which are responsible for electrolyte detachment and, along with AM cracking, are another critical factor contributing to mechanical degradation. Detachment between two cohesive surfaces is promoted by shear and normal

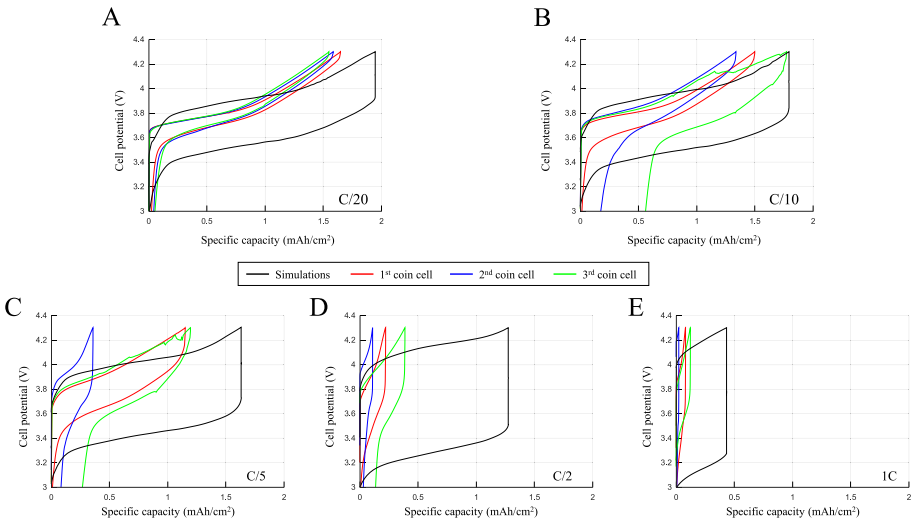

Fig. 6. Comparison between numerical and experimental cell performance:(A-E) Comparison between the cyclic voltammetry results of the simulated (black curves) and experimental (red, blue and green curves) cells operating at different C-rates.

tensile stresses [38,39]: analysis of the interfacial stresses between the AM and SPE is fundamental to predict cell failure. Fig. 5C-D shows the interfacial normal and shear stresses, which are mostly localized around the AM-binder interface. While the contribution to the shear stresses is similar regardless of the binder orientation (panel D), the normal stresses show both compressive and tensile behavior depending on the position of the AM particle and the main binder orientation (panel C). Therefore, the combined surface stresses are not homogeneous throughout the cell and, as observed experimentally, part of the SPE is more likely to detach, leading to inhomogeneities in cell behavior as degradation progresses. When combined with a detailed characterization of the mechanical behavior of the AM and a quantitative assessment of the cohesion between the SPE and the NMC, this analysis could be used to relate the stress distribution to capacity fade and thus predict the performance loss in subsequent cycles. Note that these simulations were performed under the assumption of optimal infiltration and homogeneous SPE properties: clearly, the addition of voids or inhomogeneous SPE properties would affect the results obtained. This assumption is expected to lead to an overestimation of the cell performance with respect to the experimental counterpart. However, this assumption is useful to provide an estimation of the potential of the proposed architecture regardless of the limitations due to a preliminary, laboratory-level infiltration processes.

Comparison between experimental and simulated voltammetries

The voltage-capacity curves obtained from the voltammetry tests are shown in Fig. 6, showing a representative discharge cycle for each coin cell per current considered (red, blue and green curves); these results are compared with the corresponding numerical curves (black data). The performance difference observed in Fig. 2B is reflected in different voltammetry profiles: e.g. the 3rd cell has a lower coulombic efficiency and the 2nd cell has a lower storage capacity. Comparing the experimental and numerical curves, the developed 3D microstructure is able to approximate the cell performance with good accuracy; the overestimated cell capacity was expected from the hypothesis of ideal cathode impregnation. The main difference between experiments and simulations is the potential drop observed when the applied current is reversed, higher for the numerical curves. This difference is probably due to (i) an overestimation of the ionic resistance of the compressed SPE layers, probably expelled laterally during cell sealing, and (ii) an underestimation of the electrical conductivity of the composite cathode. The latter could be related to the combined hypotheses of non-overlapping particles and sparse distribution of CB on the AM surface, which creates severe bottlenecks for electron transport between adjacent particles, as already discussed in Setion “Simulated cathode microstructures: analysis and key properties”: dedicated characterizations could provide further insights to improve the model representativity in this direction.

Despite these limitations, the model is shown to recover the experimental cell behavior, especially at low currents, and can be used to estimate the ideal upscaled cell performance via the EECM model.

Equivalent circuit model

Microscale-resolved electrochemical models offer great accuracy and insight into the operating cell, as demonstrated in Setion “Simulated cathode microstructures: analysis and key properties”, but are computationally expensive, limiting their suitability for many applications that require near-real-time predictions. Linking the microstructure model to the equivalent electrical circuit (EECM) would create a self-consistent simulation framework, bridging the cell architecture with a fast and simple 0D model while maintaining high accuracy. To this end, the 3D electro-chemo-mechanical model was used to retrieve the EECM parameters as a function of the average relative lithium concentration in the NMC θ (see Methods). At the same time, dedicated HPPC tests on the coin cell are used to calibrate the EECM parameters to experimental data, allowing the two predictions to be compared.

The battery was initially considered as fully charged at 4.3 V and progressively discharged with pulses of C/10, corresponding to 2.081 A/m^2, allowing a relaxation time > 5000 s after the current is switched off. The results show, as expected, a low dependence on θ, considering that in the implemented 3D model only the equilibrium potential and the AM volumetric expansion depend on this parameter. Considering the first RC branch, the $R_{p,1}$ decreases with increasing θ, while C_1 tends to increase. Instead, the second RC branch behaves almost as a resistor, with capacitance values 5 orders of magnitude lower than the former. As a consequence, the cell behavior could be represented by an equivalent circuit with a single RC branch: the resulting model parameters are reported in Table 2. Fig. 7A compares the simulated (blue data) and fitted (red data) rescaled relaxation voltage curves for $\theta = 0.856$, showing good agreement as also confirmed by the low values of root mean squared errors, 4.2% for all the considered values of θ when considering a one-RC branch model.

The experimental EECM parameters representative of the considered cell are also obtained via a pulsed discharge test: 11 voltage relaxation curves are interpreted with a single RC branch, in line

Table 2
EECM parameters fitten on simulation data. Equivalent circuit model parameters fitted via Eq. (4) on θ-dependent relaxation curves simulated with the 3D electro-chemo-mechanical model during a pulsed discharge at C/10.

θ	0.428	0.455	0.492	0.584	0.674	0.856
R_s (10^{-2} Ωm^2)	10.804	10.811	10.777	10.709	10.706	10.799
$R_{p,1}$ (10^{-2} Ωm^2)	1.240	1.318	1.078	0.560	0.527	0.510
C_1 (10^4 F/m^2)	2.099	2.783	3.815	7.562	8.559	8.975

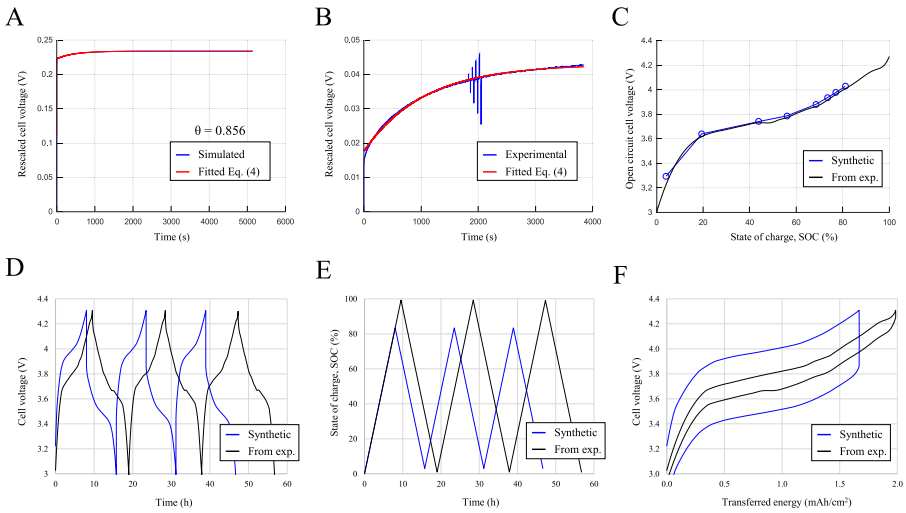

Fig. 7. Equivalent electrical circuit modeling: (A-B) Comparison between the measured (blue data) and fitted (red data) rescaled cell voltage for the simulated (panel A) and experimental (panel B) cells during pulsed discharge tests. Only a single coin cell was considered for this test. The curves show one of the relaxation transients obtained and used to fit the EECM parameters via Eq. (4). **(C)** Open circuit voltage obtained from the simulated (blue data) and experimental (black curve) pulsed discharge test. The x-asis was obtained by normalizing θ with respect to a considered available window of 0.258 – 1, resulting in the standard definition of the cell state of charge (SOC). **(D-E)** Time-dependent cell voltage (panel D) and available capacity (panel E) obtained from the EECM simulations either considering the set of parameters fitted on the simulation data (blue curve, fitting shown in panel A) or on the experimental relaxation curves (black curve, fitting shown in panel B). **(F)** Comparison between the obtained cell potential as a function of the transferred specific capacity obtained via EECM simulations. The results shown in panels D-F were obtained considering a cell with nominal capacity of 3.54 mAh and applying a current of 0.35 mA, corresponding to C/10.

with the results reported above. Fig. 7B shows one of the obtained rescaled ralaxation cell voltages (blue curve) and the corresponding fitted curve (red data): all fitted curves showed excellent good agreement, with an RMSE below 1%. The fitted EECM parameters show no significant dependence with respect to θ, resulting, by averaging, in $R_s = (1.3 \pm 0.3) \cdot 10^{-2}\ \Omega\,m^2$, $R_{p,1} = (1.7 \pm 0.3) \cdot 10^{-2}\ \Omega\,m^2$, and $C_1 = (6.3 \pm 1.7) \cdot 10^4\ F/m^2$. The two parameters sets are comparable and describe cells with slightly different behavior. The simulated data resulted in approximately one order of magnitude higher values of internal resistance, also consistent with the cell behavior shown in Fig. 6. This was expected by comparing the relaxation curves shown in Figs. 7A-B: although the simulated and experimental tests were performed with marginally different applied currents (2.08 A/m^2 and 1.31 A/m^2, respectively), the simulated voltage drop is about 10 times higher than that of the manufactured cell. This is consistent with the analysis of the simulated cathode properties and performance in Sections “Simulated cathode microstructures: analysis and key properties”–“3D-resolved full-cell simulations”, the obtained high electrical resistance is due to the low connectivity provided by the distribution of the carbon material on the AM surface. Instead, the values of capacitance obtained are coherent. Fig. 7C compares the experimental (black curve) and simulated (blue data) open circuit voltages obtained from the pulsed discharge tests. The x-axis indicates the cell state of charge (SOC), obtained by normalized the considered values of θ with respect to the available window granted by the NMC622, namely in the range 0.25–1 (see Fig. 4B). The two curves obtained show good agreement along the whole cell capacity range considered. The two sets of fitted parameters were used to simulate three charge/discharge cycles of cells with a nominal capacity of 3.54 mAh at C/10, consistent with the manufactured coin cells. Note that the uncertainty of the experimentally fitted parameters was not accounted for in these simulations. Fig. 7D shows the time-dependent cell potentials: the synthetic parameters (blue curve) result in higher ohmic losses, leading to shorter cycles compared to those obtained with the experimentally fitted parameters (black curve). This is also reflected in a better utilization of the available cell charge (see Fig. 7E): the synthetic parameters enable the of use only 80% of the available charge, lower than the almost 100% of the experimental parameter set. Nevertheless, the accuracy of the EECM predictions is best shown by comparing Fig. 7F with the results of the voltammetry tests shown in Fig. 6B. The model-derived curve is almost identical to that obtained from the 3D electrochemical model, thus maintaining good fidelity with respect to the original data set; instead, the experimentally derived parameters tend to overestimate the cell performance, although they still capture trends similar to those observed in the best-performing coin cell tested (1st, coin cell, red data in Fig. 6).

Overall, the comparison between the experimental and simulated EECM parameters demonstrates good agreement, particularly within the limits of the original modeling assumptions, such as the prediction of higher electrical resistance than that observed in the tested coin cells. The approach presented effectively bridges the two modeling scales: transitioning from 3D to 0D simulations enables accurate predictions of cell performance while maintaining high fidelity to the original predictions.

Conclusions

This work integrates experimental characterization and numerical modeling to evaluate the performance of an all-solid-state Li-ion cell using a novel solid polymer electrolyte (SPE). Stand-alone SPE sheets are tested in a pressure-controlled symmetric cell, resulting in good elasticity (Young’s modulus of 8–10 MPa), high ionic conductivity

(peak value of 0.9 mS/cm), adequate Li diffusivity and transfer coefficient (peak values of $7{\cdot}10^{-8}$ cm^2/s and 0.22, respectively), with moderate dependence on applied pressure. Despite the successful incorporation of SPE into NMC-based coin cells, the lab-scale impregnation process led to inhomogeneous cathode impregnation, causing inconsistent cell performance and reduced discharge capacity. To predict the maximum cell performance with optimal SPE infiltration, a 3D-resolved microstructure model of the composite cathode is obtained using a stochastic algorithm. First, key average properties are evaluated over a sample of 30 structures include percentage of NMC available for intercalation (~98%), active NMC surface area (~50%), electrical conductivity ($\sim 4{\cdot}10^{-2}$ S/m), and ionic tortuosity (1.7). Then, leveraging the measured SPE transfer properties, coupled electrochemical–mechanical simulations are used to predict cell behavior operating with currents ranging from C/20 to 1C, and to assess possible sources of mechanical ageing in terms of material failure and NMC-SPE detachment. Compared to the experimental voltammetry results, the model showed good agreement with experimental results at low currents (C/20, C/10), though discrepancies, as expected, arose at higher currents. Finally, the study also demonstrated the feasibility of using the microstructure model to estimate parameters for an equivalent electrical circuit model, facilitating more efficient simulations calibrated on the accurate results obtained by 3D simulations. The numerical and experimental results were consistent, with capacitance around $3 \cdot 10^4$ F/m^2 and total cell resistance on the order of 10^{-2} $\Omega\,m^2$, although the model slightly overestimated resistance due to assumptions discussed above ($\sim 10^{-1}$ $\Omega\,m^2$). The resulting EECM dis/charge curves obtained with the model-derived parameters closely matched the original data set, demonstrating high fidelity. In contrast, the curves obtained with the experimentally derived parameters also showed good agreement, although with a moderate overestimation of the cell capacity. While the proposed multiscale modeling framework provides valuable insights into electrode performance and suggests the impact of microstructure on cell performance, it is not without limitations. The model simplifies certain microstructural features, such as carbon black distribution and particle connectivity, which may reduce its accuracy in fully capturing electrode behavior. In addition, localized mechanical failures and long-term aging phenomena are not included in the present framework, limiting its applicability to short-term performance predictions. Furthermore, the computational requirements of the simulations limit their use in large-scale parametric or long-term studies. Despite these limitations, our framework provides a predictive and material-driven approach that provides a robust foundation for advancing electrode design and performance optimization. Future work will focus on enhancing the mechanical aging predictions through additional experimental data on mechanical and adhesion properties of the materials, integrating imaging data to improve microstructural representativeness, incorporating submodels for aging and mechanical failure, and refining the model's accuracy regarding effective cathode properties by comparison with dedicated high-resolution electrode models.

In conclusion, this study presents a practical case study of how experimental and microscale numerical models can be used to assess and predict the performance of novel all-solid-state architectures. The proposed multiscale modeling framework can be leveraged to provide accurate details on the internal cell behavior without requiring expensive characterization techniques, support the development of upper-scale system-level models, and, overall, foster its use in real-world applications.

List of acronyms

- CB: Carbon-Based additive
- CMC: Carboxymethyl cellulose
- EECM: Equivalent Electrical Circuit Model
- EIS: Electrochemical Impedance Spectroscopy
- FEM: Finite Elements Method
- HPPC: Hybrid Pulse Power Characterization
- NMC: Nickel Manganese Cobalt Oxide, referring to NMC622
- PSD: Particles Size Distribution
- SEM: Scanning Electron Microscopy
- SOC: State Of Charge
- SPE: Solid Polymer Electrolyte

CRediT authorship contribution statement

Matteo Alberghini: Writing – original draft, Visualization, Validation, Software, Methodology, Investigation, Formal analysis, Data curation, Conceptualization. **Giulia Blanco:** Visualization, Software, Investigation, Formal analysis. **Ashutosh Agrawal:** Writing – original draft, Visualization, Methodology, Investigation, Formal analysis, Data curation. **Pasquale Romano:** Visualization, Investigation, Formal analysis, Data curation. **Mattia Giuliano:** Methodology, Investigation. **Franklin Seute:** Methodology, Investigation. **Daniele Di Lecce:** Validation, Methodology, Investigation. **Ishamol Shaji:** Visualization, Methodology, Investigation. **Giovanna Nicol:** Supervision, Resources, Project administration, Methodology, Funding acquisition, Conceptualization. **Alix Ladam:** Project administration, Methodology, Investigation. **Sebastien Fantini:** Supervision, Resources, Project administration, Methodology, Funding acquisition, Conceptualization. **Mohammadhosein Safari:** Supervision, Resources, Project administration, Methodology, Funding acquisition, Conceptualization. **Philippe M. Vereecken:** Supervision, Resources, Project administration, Funding acquisition, Conceptualization. **Alessio Tommasi:** Supervision, Resources, Project administration, Methodology, Funding acquisition, Conceptualization.

Declaration of competing interest

The authors declare that they have no known competing financial interests or personal relationships that could have appeared to influence the work reported in this paper.

Acknowledgments

This research was performed within the SOLiDIFY project, funded by the European Union's Horizon 2020 research and innovation program under grant agreement No. 875557. We acknowledge the contribution of Sidrabe Vacuum SIA and Fraunhofer ISC for the supply of part of the cell components.

Data availability

Data will be made available on request.

References

[1] X.-X. Zeng, Y.-X. Yin, N.-W. Li, W.-C. Du, Y.-G. Guo, L.-J. Wan, Reshaping lithium plating/stripping behavior via bifunctional polymer electrolyte for room-temperature solid li metal batteries, J. Am. Chem. Soc. 138 (49) (2016) 15825–15828.

[2] H. Wang, L. Sheng, G. Yasin, L. Wang, H. Xu, X. He, Reviewing the current status and development of polymer electrolytes for solid-state lithium batteries, Energy Storage Mater. 33 (2020) 188–215.

[3] C. Fu, G. Homann, R. Grissa, D. Rentsch, W. Zhao, T. Gouveia, A. Falgayrat, R. Lin, S. Fantini, C. Battaglia, A polymerized-ionic-liquid-based polymer electrolyte with high oxidative stability for 4 and 5 V class solid-state lithium metal batteries, Adv. Energy Mater. 12 (27) (2022) 2200412.

[4] H. Liu, X.-B. Cheng, J.-Q. Huang, H. Yuan, Y. Lu, C. Yan, G.-L. Zhu, R. Xu, C.-Z. Zhao, L.-P. Hou, et al., Controlling dendrite growth in solid-state electrolytes, ACS Energy Lett. 5 (3) (2020) 833–843.

[5] C. Sun, J. Liu, Y. Gong, D.P. Wilkinson, J. Zhang, Recent advances in all-solid-state rechargeable lithium batteries, Nano Energy 33 (2017) 363–386.

[6] V. Nagda, A. Kulachenko, S.B. Lindström, Image-based 3D characterization and reconstruction of heterogeneous battery electrode microstructure, Comput. Mater. Sci. 223 (2023) 112139.

[7] B.L. Trembacki, A.N. Mistry, D.R. Noble, M.E. Ferraro, P.P. Mukherjee, S.A. Roberts, Mesoscale analysis of conductive binder domain morphology in lithium-ion battery electrodes, J. Electrochem. Soc. 165 (13) (2018) E725–E736.
[8] K. Higa, S.-L. Wu, D.Y. Parkinson, Y. Fu, S. Ferreira, V. Battaglia, V. Srinivasan, Comparing macroscale and microscale simulations of porous battery electrodes, J. Electrochem. Soc. 164 (11) (2017) E3473.
[9] S. Hein, T. Danner, D. Westhoff, B. Prifling, R. Scurtu, L. Kremer, A. Hoffmann, A. Hilger, M. Osenberg, I. Manke, et al., Influence of conductive additives and binder on the impedance of lithium-ion battery electrodes: effect of morphology, J. Electrochem. Soc. 167 (1) (2020) 013546.
[10] T. Danner, M. Singh, S. Hein, J. Kaiser, H. Hahn, A. Latz, Thick electrodes for Li-ion batteries: A model based analysis, J. Power Sources 334 (2016) 191–201.
[11] M. Alberghini, G. Blanco, A. Bertinetti, A. Tommasi, M. Sgroi, A simplified 3D-resolved microstructure model for high-fidelity lithium-ion battery cell simulations, J. Power Sources 613 (2024) 234817.
[12] A. Bielefeld, D.A. Weber, J. Janek, Microstructural modeling of composite cathodes for all-solid-state batteries, J. Phys. Chem. C 123 (3) (2018) 1626–1634.
[13] A. Bielefeld, D.A. Weber, J. Janek, Modeling effective ionic conductivity and binder influence in composite cathodes for all-solid-state batteries, ACS Appl. Mater. Interfaces 12 (11) (2020) 12821–12833.
[14] A. Bielefeld, D.A. Weber, R. Rueß, V. Glavas, J. Janek, Influence of lithium ion kinetics, particle morphology and voids on the electrochemical performance of composite cathodes for all-solid-state batteries, J. Electrochem. Soc. 169 (2) (2022) 020539.
[15] M. Clausnitzer, R. Mücke, F. Al-Jaljouli, S. Hein, M. Finsterbusch, T. Danner, D. Fattakhova-Rohlfing, O. Guillon, A. Latz, Optimizing the composite cathode microstructure in all-solid-state batteries by structure-resolved simulations, Batter. Supercaps 6 (11) (2023) e202300167.
[16] C. Sangrós Giménez, C. Schilde, L. Froböse, S. Ivanov, A. Kwade, Mechanical, electrical, and ionic behavior of lithium-ion battery electrodes via discrete element method simulations, Energy Technol. 8 (2) (2020) 1900180.
[17] C.S. Giménez, B. Finke, C. Nowak, C. Schilde, A. Kwade, Structural and mechanical characterization of lithium-ion battery electrodes via DEM simulations, Adv. Powder Technol. 29 (10) (2018) 2312–2321.
[18] J. Evans, C.A. Vincent, P.G. Bruce, Electrochemical measurement of transference numbers in polymer electrolytes, Polymer 28 (13) (1987) 2324–2328.
[19] P.G. Bruce, C.A. Vincent, Steady state current flow in solid binary electrolyte cells, J. Electroanal. Chem. Interfacial Electrochem. 225 (1–2) (1987) 1–17.
[20] D.M. Pesko, K. Timachova, R. Bhattacharya, M.C. Smith, I. Villaluenga, J. Newman, N.P. Balsara, Negative transference numbers in poly (ethylene oxide)-based electrolytes, J. Electrochem. Soc. 164 (11) (2017) E3569.
[21] F. Silveri, M. Alberghini, V. Esnault, A. Bertinetti, V. Rouchon, M. Giuliano, G. Gudendorff, C. Zhao, J. Bikard, M. Sgroi, et al., Multiscale modelling of Si based Li-ion battery anodes, J. Power Sources 598 (2024) 234109.
[22] W. Mei, Q. Duan, P. Qin, J. Xu, Q. Wang, J. Sun, A three-dimensional electrochemical-mechanical model at the particle level for lithium-ion battery, J. Electrochem. Soc. 166 (14) (2019) A3319.
[23] Y. Zhao, P. Stein, Y. Bai, M. Al-Siraj, Y. Yang, B.-X. Xu, A review on modeling of electro-chemo-mechanics in lithium-ion batteries, J. Power Sources 413 (2019) 259–283.
[24] V. Malavé, J. Berger, P. Martin, Concentration-dependent chemical expansion in lithium-ion battery cathode particles, J. Appl. Mech. 81 (9) (2014) 091005.
[25] R.M. Santos, C.L.d.S. Alves, E.C. Macedo, J.M. Villanueva, L.V. Hartmann, Estimation of lithium-ion battery model parameters using experimental data, in: 2017 2nd International Symposium on Instrumentation Systems, Circuits and Transducers, INSCIT, IEEE, 2017, pp. 1–6.
[26] Z. Li, J. Fu, X. Zhou, S. Gui, L. Wei, H. Yang, H. Li, X. Guo, Ionic conduction in polymer-based solid electrolytes, Adv. Sci. 10 (10) (2023) 2201718.
[27] Z. Song, X. Wang, H. Wu, W. Feng, J. Nie, H. Yu, X. Huang, M. Armand, H. Zhang, Z. Zhou, Bis (fluorosulfonyl) imide-based electrolyte for rechargeable lithium batteries: A perspective, J. Power Sources Adv. 14 (2022) 100088.
[28] H. Sun, Q. Yang, D. Kong, Y. Li, Y. He, N. Zhang, H. Hu, Effect of thermal pre-compressing on ionic conductivity and mechanical properties of PEO-based solid-state electrolytes, J. Appl. Polym. Sci. 141 (44) (2024) e56156.
[29] S. Berg, T. Kelly, I. Porat, B. Moradi-Ghadi, H. Ardebili, Mechanical deformation effects on ion conduction in stretchable polymer electrolytes, Appl. Phys. Lett. 113 (8) (2018).
[30] A. Agrawal, S. Yari, H. Hamed, T. Gouveia, R. Lin, M. Safari, Synergistic interactions between the charge-transport and mechanical properties of the ionic-liquid-based solid polymer electrolytes for solid-state lithium batteries, Carbon Energy 5 (11) (2023) e355.
[31] P. Barai, K. Higa, V. Srinivasan, Impact of external pressure and electrolyte transport properties on lithium dendrite growth, J. Electrochem. Soc. 165 (11) (2018) A2654.
[32] M. Doyle, T.F. Fuller, J. Newman, Modeling of galvanostatic charge and discharge of the lithium/polymer/insertion cell, J. Electrochem. Soc. 140 (6) (1993) 1526.
[33] B. Tjaden, S.J. Cooper, D.J. Brett, D. Kramer, P.R. Shearing, On the origin and application of the bruggeman correlation for analysing transport phenomena in electrochemical systems, Curr. Opin. Chem. Eng. 12 (2016) 44–51.
[34] P. Liu, R. Xu, Y. Liu, F. Lin, K. Zhao, Computational modeling of heterogeneity of stress, charge, and cyclic damage in composite electrodes of Li-ion batteries, J. Electrochem. Soc. 167 (4) (2020) 040527.
[35] M. Duquesnoy, T. Lombardo, M. Chouchane, E.N. Primo, A.A. Franco, Data-driven assessment of electrode calendering process by combining experimental results, in silico mesostructures generation and machine learning, J. Power Sources 480 (2020) 229103.
[36] D.-W. Chung, M. Ebner, D.R. Ely, V. Wood, R.E. García, Validity of the bruggeman relation for porous electrodes, Modelling Simul. Mater. Sci. Eng. 21 (7) (2013) 074009.
[37] N.-S. Choi, S.-Y. Ha, Y. Lee, J.Y. Jang, M.-H. Jeong, W.C. Shin, M. Ue, Recent progress on polymeric binders for silicon anodes in lithium-ion batteries, J. Electrochem. Sci. Technol. 6 (2) (2015) 35–49.
[38] P.P. Camanho, C.G. Davila, M. De Moura, Numerical simulation of mixed-mode progressive delamination in composite materials, J. Compos. Mater. 37 (16) (2003) 1415–1438.
[39] N. Iqbal, Y. Ali, S. Lee, Analysis of mechanical failure at the interface between graphite particles and polyvinylidene fluoride binder in lithium-ion batteries, J. Power Sources 457 (2020) 228019.